# First-principles study of phonon properties in magnetic double-layer manganites

O. De la Peña-Seaman,[1,2] R. Heid,[1] and K.-P. Bohnen[1]

[1]*Institut für Festkörperphysik, Karlsruher Institut für Technologie (KIT), P.O. Box 3640, D-76021 Karlsruhe, Germany*

[2]*Instituto de Física, Benemérita Universidad Autónoma de Puebla, Apartado postal J-48, 72570, Puebla, Pue., México*

(Received 27 April 2012; published 5 July 2012)

We have studied the lattice dynamical properties of the tetragonal double-layer manganite system $La_{2-2x}Sr_{1+2x}Mn_2O_7$ ($x = 0.4$) within the framework of density functional perturbation theory, using a mixed-basis pseudopotential method and the virtual-crystal approximation for modeling the alloy. Performing phonon dispersion calculations for both ferromagnetic (FM) and nonmagnetic (NM) ground states in the plane $q_z = 0$ revealed a strong influence of the magnetic order on high-frequency modes which involve oxygen vibrations with Mn-O bond-stretching modulations. They can be traced back to changes in the dynamical coupling of medium-ranged bonds like Mn-Mn or O-O, while the nearest-neighbor Mn-O bonds remain practically unchanged. Electronically they originate from a replacement of the predominant Mn $d(t_{2g})$ orbital polarization in the NM phase by a $d(e_g)$-type polarization in the FM phase. Good agreement is found between theoretical predictions for phonon frequencies and intensities in the [110] direction and a previous neutron scattering experiment performed in the FM phase. Finally, calculations of the electron-phonon interaction revealed that dips in the dispersion of the high-frequency bond-stretching branches are connected to an enhanced electron-phonon coupling, but on average only a moderate coupling constant of $\lambda = 0.65$ is obtained.

DOI: 10.1103/PhysRevB.86.014301 PACS number(s): 75.47.Lx, 71.15.Mb, 63.20.D−, 63.20.kd

## I. INTRODUCTION

Since the discovery of the colossal magnetoresistance (CMR) effect in ferromagnetic (FM) manganites[1,2] the interest in these materials has been renewed. One of the key outstanding problems, among others, is the understanding of the nature of the metal-insulator transition at the Curie temperature ($T_C$), a transition that is distinctly different to those of ordinary ferromagnetic metals such as Fe, Co, or Ni. Here, the interplay between charge, spin, and lattice degrees of freedom in manganites results in a multitude of unconventional properties of fundamental as well as practical interest.[3,4]

Manganites crystallize in perovskite-derived structures with compositions of the so-called Ruddlesden-Popper type $(R,A)_{n+1}Mn_nO_{3n+1}$, where R and A denote trivalent rare-earth and divalent alkaline-earth ions, respectively, and $n$ indicates the number of layers per unit cell. The majority of studies have been devoted to the cubic manganites $R_{1-x}A_xMnO_3$ ($n = \infty$, R = Sr,Ca), where Mn sits in the center of an oxygen octahedron. Depending on the composition they show a variety of magnetic and electronic phenomena, including ferromagnetic, antiferromagnetic, charge, and orbital ordering. This complex behavior is related to the presence of both $Mn^{3+}$ and $Mn^{4+}$ ions, whose concentrations are controlled by the doping level $x$. The $Mn^{3+}$ ions are Jahn-Teller (JT) active, which favors a localization of the Mn $e_g$ electron, while the presence of $Mn^{4+}$ ions supports a higher mobility. The subtle balance between these two trends drives the various phase transitions.[3,4]

Recently, more attention has been devoted to $La_{2-2x}Sr_{1+2x}Mn_2O_7$ double-layer manganites (space group $I4/mmm$, No. 139).[6,7] The crystal structure of this layered compound, shown in Fig. 1, consists of two neighboring $MnO_2$ sheets ($MnO_2$ bilayer) alternately stacked with $(La,Sr)_2O_2$ layers along the $c$ axis.[6,7] At compositions close to $x = 0.5$ ($LaSr_2Mn_2O_7$) the La and Sr atoms tend to separate into different layers. The La layer lies in the middle of the $MnO_2$ bilayer (2$b$ sites), while Sr occupies two layers between adjacent $MnO_2$ bilayers (4$e$ sites).[6] At low temperatures a metallic FM phase exists in the doping range $0.3 \leqslant x \leqslant 0.4$. However, at the Curie temperature ($T_C \approx$ 130 K) the system transits to a paramagnetic insulating phase, where the breakdown of the ferromagnetism is accompanied by an increased localization of the carriers and thus by a resistivity increase. In this region the CMR effect is observed, because the application of a magnetic field just above the transition temperature stabilizes the ferromagnetic phase and thereby lowers the resistivity by orders of magnitude.[3,8–10] In the same doping range, strong coupling between electronic quasiparticles and bond-stretching phonons at low temperatures has been identified in a combined angle-resolved photoemission and inelastic neutron scattering experiment, showing that a sizable electron-phonon (e-ph) coupling exists also in the metallic ferromagnetic phase of the double-layer compound.[11,12]

The lattice dynamics of this alloy in the ferromagnetic metallic phase (at 10 K) has been investigated by inelastic neutron scattering spectroscopy along the [$\xi\xi$0] direction.[12] Constant-$Q$ scans between 40 and 80 meV (focusing mainly on the Mn-O phonon modes) together with shell model calculations classified the branches as bond-stretching (high energy) or bond-bending (low energy) behavior. Furthermore, a dip in the dispersion and a maximum in the linewidth for the transverse and longitudinal high-frequency branches in the range $0.25 < \xi < 0.30$ was observed. This was interpreted as an indication of strong e-ph coupling deep in the metallic state, suggesting the close relationship between the polaronic insulating phase and the phonon renormalization in the metallic phase.[12]

From the theoretical point of view, the band-structure approach based on local spin-density functional approximation (LSDA) has been rather successful in describing ground-state properties of pseudocubic manganites. For example, the

 

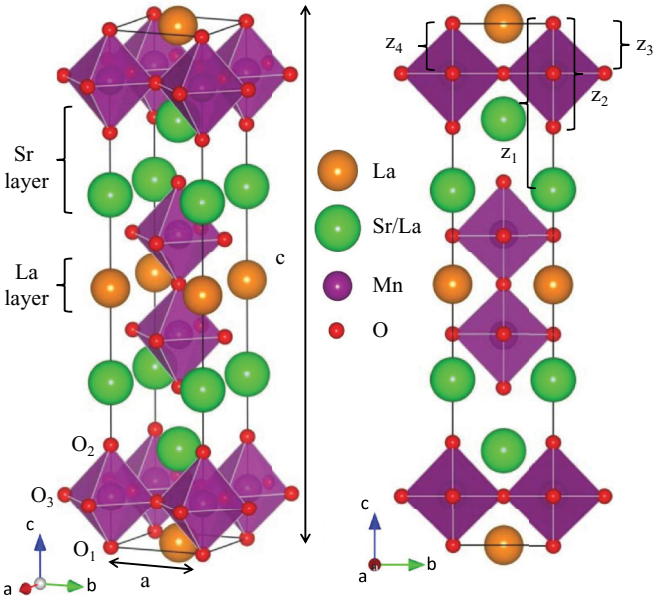


FIG. 1. (Color online) $La_{2-2x}Sr_{1+2x}Mn_2O_7$ crystal structure (Ref. 5).

antiferromagnetic ground state of the undoped $LaMnO_3$ is obtained correctly if the structural distortion of the cubic cell into a *Pnma* orthorhombic structure is properly taken into account.[13,14] Good agreement even with excited-state properties has been noted.[14] Using supercell and virtual-crystal approaches, the FM phase at $x \approx 1/3$ is also reasonably well described in LSDA as an itinerant ferromagnet.[13,15] With regard to the bilayer manganites, there exist only a few theoretical studies which focus on the electronic and magnetic properties for a narrow composition range ($0.36 \leqslant x \leqslant 0.5$). They comprise several different approaches such as a full-potential linearized augmented plane wave method,[16–18] a full-potential linear muffin tin orbital method,[19] and an all-electron fully charge and spin self-consistent Korringa-Kohn-Rostoker framework.[17,20] All these studies agree that the electronic structure near $E_F$ is dominated by the Mn $d(e_g)$ and Mn $d(t_{2g})$ states for the majority and minority spin channel, respectively, and that the band structure shows a very small dispersion along the $c$ direction. Even finer details like a minority spin pocket at $\Gamma$ have been obtained, which is supported by angle-resolved photoemission spectroscopy.[20] These results demonstrate the applicability of LSDA to manganites, and suggest that correlation effects due to the Mn $3d$ shell are of minor importance. However, a theoretical characterization of the lattice dynamics as well as of the interplay between electronic and lattice degrees of freedom within the DFT framework is still lacking.

In this paper we present a study of the lattice dynamical and electron-phonon coupling properties of the tetragonal double-layer manganite $La_{2-2x}Sr_{1+2x}Mn_2O_2$ within the framework of density functional perturbation theory[21] using a mixed-basis pseudopotential method.[22] We will focus on the composition $x = 0.4$ and treat the nonstoichiometry of the La/Sr alloy in the self-consistent virtual-crystal approximation (VCA),[23] which was successfully applied to pseudocubic manganites.[13,15] The vibrational properties are obtained with the linear response theory,[24–28] a very efficient approach for the calculation of lattice dynamical properties. We give a detailed description and analysis of the phonon dispersion for the $[\xi 00]$ and $[\xi\xi 0]$ high-symmetry directions as well as related e-ph coupling properties and discuss them in the light of recent measurements. Spin-polarization effects on the vibrational properties, specifically on the phonon frequencies and eigenvectors of the high-energy bond-stretching branches are discussed in detail as well. The overview of the paper is the following: In Sec. II we describe the computational details of our calculations. In Secs. III A and III B we present results of the effect of magnetism on phonon dispersion and force constants. A comparison with experimental data and structure factor calculations as well as electron-phonon coupling analysis are discussed in Secs. III C and III D, respectively. In Sec. IV the main findings are summarized.

## II. COMPUTATIONAL DETAILS

The non- and spin-polarized calculations were performed with the mixed-basis pseudopotential method (MBPP).[22,24] For La, Sr, Mn, and O norm-conserving pseudopotentials were constructed according to the Vanderbilt description.[29] Partial core corrections have been included in all cases and we have explicitly considered $s$ and $p$ semicore states for La, Sr, and Mn. The fairly deep potentials are efficiently treated by the mixed-basis scheme, which uses a combination of local functions and plane waves for the representation of the valence states. We used $s$-, $p$-, and $d$-type functions at the La, Sr, and Mn sites, and $s$- and $p$-type functions for O, supplemented by plane waves up to a kinetic energy of 25 Ry. Phonon properties were calculated via density functional perturbation theory[21,24] as implemented in the MBPP code.[25,27] The studies were carried out with the PBE form[30–32] for the GGA exchange-correlation functional. Brillouin-zone integration was performed with a Gaussian smearing of 0.2 eV and a $12 \times 12 \times 4$ tetragonal $k$-point mesh, which was sufficient to converge phonon frequencies to 0.2 meV. As the phonon calculations were computationally very demanding, we restricted the present study to a $4 \times 4 \times 1$ $q$-point mesh, which after Fourier interpolation allowed us to study all phonon branches of the plane $q_z = 0$. The calculation of e-ph coupling properties was done with a dense $36 \times 36 \times 12$ $k$-point mesh.

The $La_{1.2}Sr_{1.8}Mn_2O_7$ ($x = 0.4$) alloy was modeled in the self-consistent virtual-crystal approximation (VCA). In the present pseudopotential method, the VCA is implemented by generating new pseudopotentials with a fractional nuclear charge and by adjusting the valence charge accordingly.[23] As a reference compound we used $LaSr_2Mn_2O_7$ ($x = 0.5$) with ordered La and Sr sublattices as indicated in Fig. 1, where La occupies the $2b$ sites and Sr the $4e$ sites of the space group $I4/mmm$.[6] The composition with $x = 0.4$ is then modeled by replacing each Sr atom by a virtual atom with a nuclear charge increased by 0.1. This formally corresponds to a 10% exchange of Sr by Y, which is isovalent to La. Previous work on manganites has shown that this VCA scheme accurately describes the main features of the electronic structure near the Fermi level due to the fact that both La and Sr merely act as electron donors.[13,15,19] However, because of the different ionic radii of La and Y, a structural optimization via energy minimization turned out to be unreliable. We

therefore performed all calculations using the low-temperature experimental structure as determined by Kobuta *et al.*[7]: La sits at (0,0,1/2), Sr/La at (0,0,$z_1$), Mn at (0,0,$z_4$), $O_1$ at (0,0,0), $O_2$ at (0,0,$z_2$), and $O_3$ at (0,1/2,$z_3$), respectively, with $a = 3.8645$ Å, $c = 20.0650$ Å, and the following internal parameters: $z_1 = 0.3178$, $z_2 = 0.1966$, $z_3 = 0.0957$, and $z_4 = 0.0960$. We confirmed that for this structure the ferromagnetic ground state is energetically more stable than the nonmagnetic one ($\Delta E = 2.45$ eV per unit cell), and electronic band structure and density of states for the ferromagnetic phase agree well with previous theoretical studies,[18–20] thus giving confidence about the current VCA implementation. The large magnetic moment of $\mu = 3.24\mu_B$ per Mn atom corresponds to a high-spin configuration. This, together with the metallic behavior with large Mn $d(e_g)$ contribution at the Fermi level and with an important O-hybridization component, catches the main features of the double exchange model[33–36] despite the fact that in our DFT scheme we are not able to distinguish between $Mn^{+3}$ and $Mn^{+4}$ ions,[9] but describe them as an average $Mn^{+3}/Mn^{+4}$ mixture.

## III. RESULTS AND DISCUSSION

### A. Effect of magnetism on the phonon dispersion

The calculated phonon dispersion along high-symmetry directions [$\xi\xi$0] and [$\xi$00] of the $q_z = 0$ plane are shown in Fig. 2. In both cases the phonon modes fall into four different symmetry classes, $\Sigma_1$ to $\Sigma_4$ and $\Delta_1$ to $\Delta_4$, respectively. To elucidate the influence of magnetism on the various phonon modes, we compare the phonon dispersion for the FM phase (black solid lines) with those for a fictitious NM phase

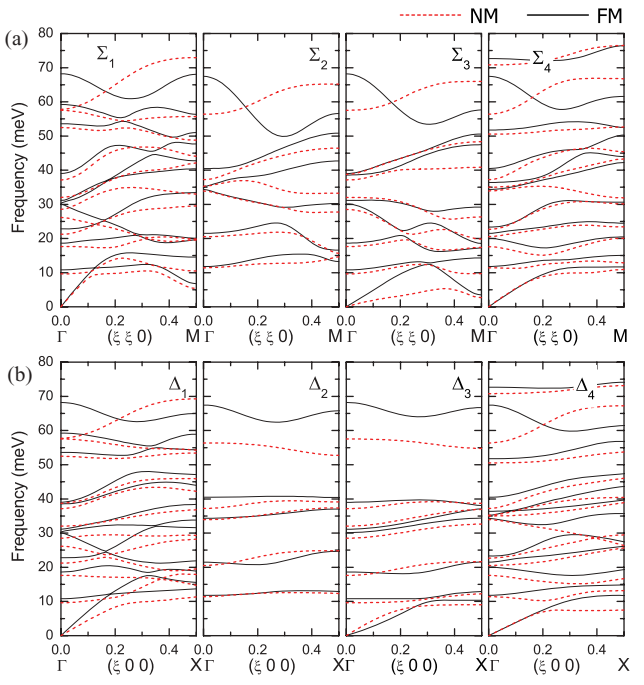


FIG. 2. (Color online) Calculated phonon dispersion of $La_{1.2}Sr_{1.8}Mn_2O_7$ for the symmetry classes (a) $\Sigma_1$ to $\Sigma_4$ along [$\xi\xi$0] and (b) $\Delta_1$ to $\Delta_4$ along [$\xi$00]. Results for the FM case (black solid lines) are compared with those from a NM calculation (red dashed lines).

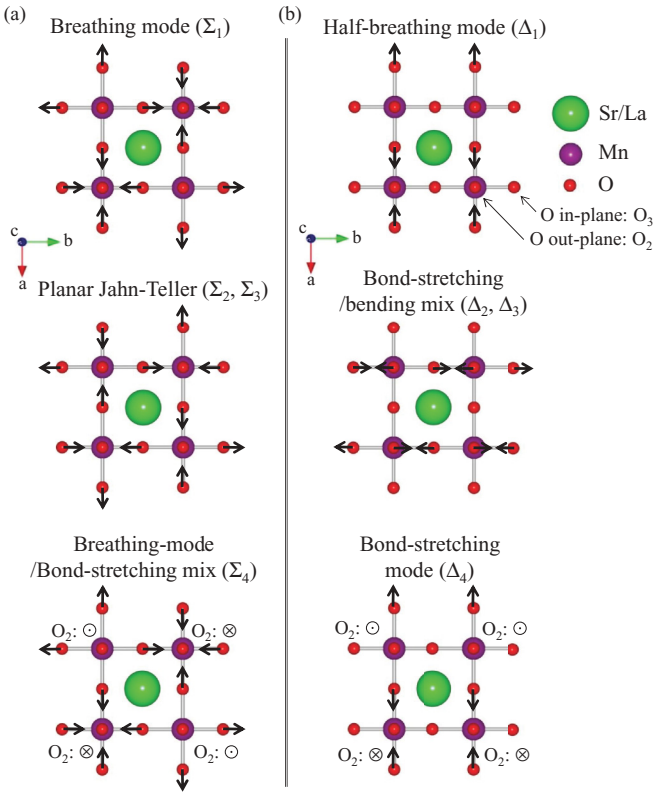


FIG. 3. (Color online) Top view of the first MnO octahedral layer showing the high-frequency phonon modes at the (a) M point and (b) X point for each symmetry class. The in-plane oxygen is denoted by $O_3$, while the out-of-plane oxygen $O_2$ sits on top of Mn.

(red dotted lines). For both cases the same experimental structure[7] has been used to allow clear identification of the effects of spin polarization on the phonon spectrum. For most branches below 50 meV the effect of spin polarization is minor and manifests itself as frequency shifts of less than 5 meV. Exceptions are some [$\xi\xi$0] bond-bending branches around 30 and 40 meV that exhibit larger shifts of ≈10 meV near the zone boundary, and a low-frequency branch of $\Sigma_3$ symmetry. The most pronounced changes occur for the high-frequency branches above 50 meV for both [$\xi\xi$0] and [$\xi$00] directions. Here inclusion of spin polarization even changes the sign of the slope of several phonon branches.

The vibrational patterns of the phonon modes with the highest frequencies (second highest for $\Sigma_4$ and $\Delta_4$) for each symmetry class at the M and X points are sketched in Figs. 3(a) and 3(b), respectively. A top view of the first MnO octahedral layer (see Fig. 1) is shown. For both high-symmetry points the eigenvectors involve almost exclusively $O_3$ *ab*-planar vibrations without any participation of Mn, Sr, or La atoms. In the case of $\Sigma_4$ and $\Delta_4$ there is also a mixing with $O_2$ (sitting just on top of Mn) vibrations along the *c* direction. The modes from $\Delta_2$ and $\Delta_3$ also show some contribution from the $O_2$ atoms with bond-bending vibration in the *b* direction. The character of the $\Sigma_1$ and $\Sigma_4$ modes is a typical *ab*-planar breathing vibration of the $O_3$ atoms, with some out-of-plane contribution for $\Sigma_4$ by $O_2$ atoms, as mentioned above. For $\Sigma_2$ and $\Sigma_3$ the modes are of *ab*-planar Jahn-Teller (quadrupolar) type, where a collinear pair of atoms moves toward Mn at

the octahedral center, while the other pair moves away from it. The $\Delta_1$ and $\Delta_4$ modes constitute a longitudinal *ab*-planar half-breathing vibration oriented along [100], again with some out-of-plane participation from the $O_2$ atoms for $\Delta_4$. Finally, for $\Delta_2$ and $\Delta_3$ the modes show a more complex pattern as a result of a combination of an $O_3$-Mn bond-stretching and an $O_2$-Mn bond-bending vibration.

### B. Force constants

In order to get a deeper microscopic understanding of why spin polarization has a particularly strong effect on these high-frequency modes, we calculated the force constant matrices related to atom-atom bonds, which characterize the strength of the dynamical coupling between a pair of atoms. They are obtained by Fourier transform of the dynamical matrices at the $4 \times 4 \times 1$ $q$-point mesh. Although this mesh is restricted to the plane $q_z = 0$, due to the long $c$ axis this procedure also gives reliable results for short-range bonds along $c$. In Fig. 4 we show a comparison of the average force constants for the FM and NM cases. The average force constant is defined by

$$I(b) = \sqrt{\frac{1}{3}\sum_{\alpha\beta}\Phi^2_{\alpha\beta}(b)}, \qquad (1)$$

where $\Phi_{\alpha\beta}(b)$ represents the force constant matrix assigned to a bond $b$. In Fig. 4 the bonds are arranged in order of increasing bond length, and the average force constants for both cases are normalized to the FM value of the shortest bond (nearest neighbor Mn-$O_1$).

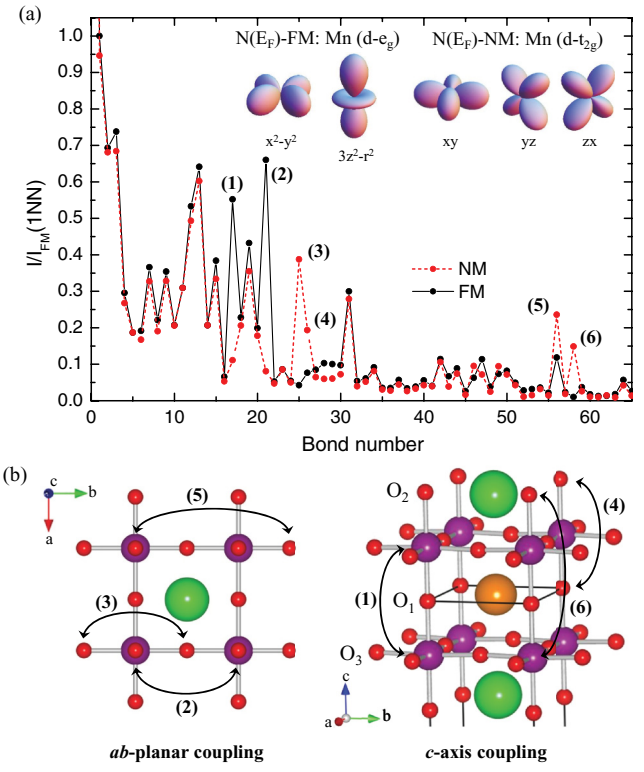


FIG. 4. (Color online) Average force constants for (a) FM (black solid line) and NM (red dashed line) phases. Bonds are ordered by increasing bond length. Each set of average force constants is normalized to the FM value of the shortest bond. Labels (1) to (6) denote those bonds which are most effected by spin polarization. (b) Cartoon of these bonds.

Spin polarization acts rather selectively on the different bonds. Large changes in dynamical couplings occur only for a small number of bonds, labeled by (1) to (6) and visualized in Fig. 4(b). Bonds (1) and (2) are out-of-plane and in-plane Mn-Mn bonds (with bond lengths 3.8525 and 3.8645 Å) which exhibit a drastic increase of the dynamical coupling in the FM phase. In contrast, the FM order leads to a large reduction of the dynamical coupling for the $O_3$-$O_3$ (in-plane) and $O_1$-$O_2$ (out-of-plane) bonds, labeled (3) and (4), respectively (with bond lengths 3.8645 and 3.9448 Å, respectively), as well as for the longer range Mn-$O_3$ and Mn-$O_2$ bonds [labels (5) and (6), with bond lengths 5.7968 and 5.8710 Å, respectively]. For all other bonds, in particular for all short Mn-O bonds [positioned to the left of bond (1) in Fig. 4(a)], the average force constants remain practically unchanged.

The modifications in the dynamical couplings can be understood from the different polarization of Mn $d$ electrons between the FM and the NM phase. In the FM case the largest contribution to the density of states at the Fermi level comes from Mn $d(e_g)$ states. In contrast, in NM the main contribution originates from Mn $d(t_{2g})$ states. The angular shape of the corresponding orbitals are depicted as an inset in Fig. 4(a). The $d(e_g)$ states are oriented along the crystallographic axes and therefore toward the nearest-neighbor oxygen atoms, while the $d(t_{2g})$ states are more isotropic and point along the main diagonals. The dominance of $d(e_g)$ states at the Fermi level in the FM phase increases on the one hand the dynamical couplings for Mn-Mn bonds, but on the other hand results in an enhanced screening of the longer O-O and Mn-O bonds with a corresponding reduction of the dynamical coupling. Thus the change of the dominant Mn $d$ states at the Fermi level by spin polarization leads to large modifications of the force constants for bonds parallel to the crystallographic axes in a nonmonotonic way, and then as a consequence to large changes in the related high-frequency phonon branches.

### C. Phonon dispersion in the ferromagnetic phase in comparison with experiments

In this section we discuss our theoretical results in the light of a previous inelastic neutron scattering experiment,[12] which focused primarily on the Mn-O bond phonon branches dispersing in the [110] direction with energies between 40 and 80 meV. In this energy range both Mn-O bond-stretching and bond-bending vibrations could be accessed. Scans have been performed in both longitudinal and transverse scattering geometries at two different Brillouin zones adjacent to $\boldsymbol{\tau} = (3,3,0)$ and $\boldsymbol{\tau} = (4,4,0)$ to obtain a better identification of the modes. Data were interpreted on the basis of a shell model.

The experimental frequencies are reproduced in Fig. 5 together with the theoretical predictions from our *ab initio* calculations. The measured phonons belong to the two representations $\Sigma_1$ (longitudinal polarization) and $\Sigma_3$ (transverse polarization), respectively. To compare with the experimental data, we have simulated the scattering intensity by calculating dynamical structure factors for total momentum transfer $\mathbf{Q} = \boldsymbol{\tau} + \mathbf{q}$, where $\mathbf{q}$ is the phonon momentum in the first

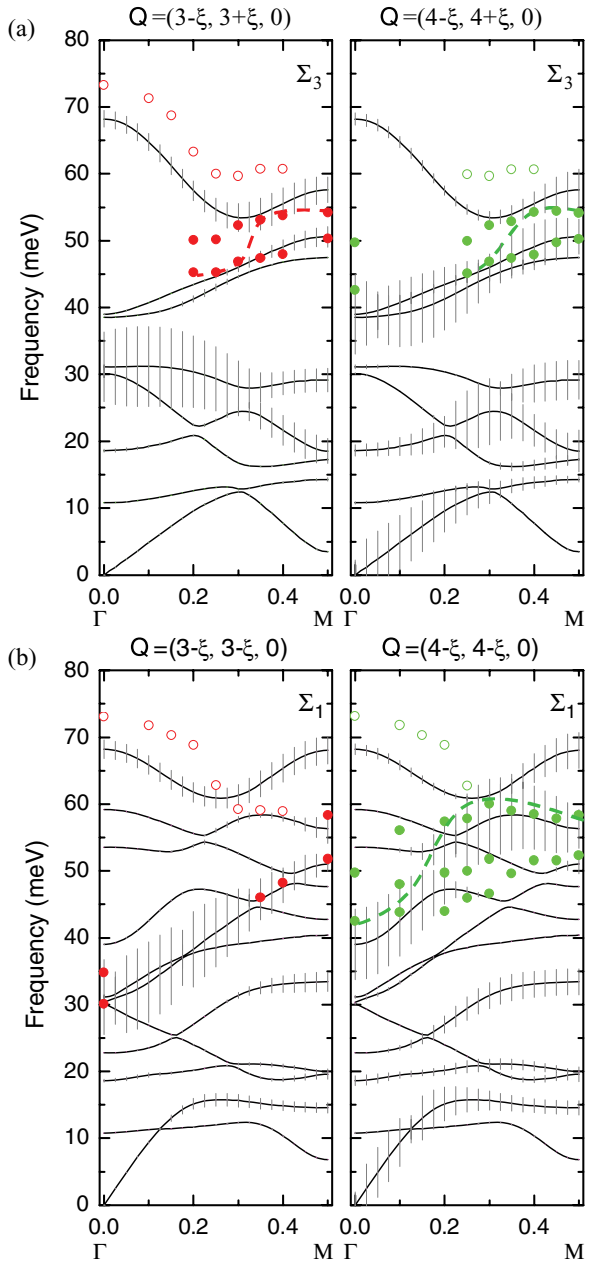


FIG. 5. (Color online) Calculated phonon dispersion (lines) for the [$\xi\xi$0] direction (a) transverse $\Sigma_3$ and (b) longitudinal $\Sigma_1$ in comparison with inelastic neutron scattering data (open circles: bond-stretching, filled circles: bond-bending modes) (Ref. 12). Dynamical structure factor calculations (vertical lines) at two reciprocal lattice points, $\boldsymbol{\tau} = (330)$ and $\boldsymbol{\tau} = (440)$, are included (where $\mathbf{Q} = \boldsymbol{\tau} + \mathbf{q}$). Dashed lines denote the dispersion of the main bond-bending spectral weight.

Brillouin zone, and $\boldsymbol{\tau}$ represents a reciprocal lattice point. Mimicking the experimental scattering condition, results for two reciprocal lattice points, $\boldsymbol{\tau} = (330)$ and $\boldsymbol{\tau} = (440)$, are shown in the left and right panels of Fig. 5, respectively, by vertical lines, which lengths are a measure for the intensity of the corresponding phonon.

The experimental finding can be summarized as follows. At the zone center ($\Gamma$ point) a bond-stretching vibration was observed at 73 meV, while other peaks located at 43 and 33 meV were identified as bond-bending vibrations. When going along [$\xi\xi$0], the transverse bond-stretching branch disperses steeply downwards, and the bending branches disperse gradually upward without overlapping until $\xi = 0.4$. Similarly, the longitudinal bond-stretching branch disperses downwards along [$\xi\xi$0], whereas the higher-energy bending mode (for the same polarization) disperses sharply upward and starts to overlap with the bond-stretching branch at $\xi \leqslant 0.3$.

In general, the theoretical frequencies are up to 5 meV softer than the measured ones, which may be due to the use of experimental lattice parameters in the calculation. For the transverse phonon dispersion $\Sigma_3$ [Fig. 5(a)], the structure factor analysis provides a clear identification of the bond-bending modes (filled symbols) lying between 40 and 55 meV, and for the bond-stretching branch (open symbols) between 60 and 75 meV. Both bond-bending branches (40–55 meV) show a monotonous hardening when going from the zone center ($\Gamma$ point) to the zone boundary (M point). However, the structure factor calculation predicts an exchange of character between the lower-frequency and the higher-frequency branch on approaching the zone boundary. This behavior can also be observed in the experimental data of Weber *et al.*[12] as a transfer of weight from the lower to the higher frequency peak, as indicated in Fig. 5(a) by the dashed lines. The calculated bond-stretching branch displays a nonmonotonous behavior, which starts with a downward dispersion from the zone center, reaches a minimum at approximately $\xi = 1/4$, and then slightly hardens towards the zone boundary. The dip structure was also found in the experiment, in connection with significantly enhanced phonon linewidths in the region of the dip. This led to the suggestion of a considerable e-ph coupling related to this branch, a question that will be discussed further in the next subsection.

For the longitudinal phonons which belong to representation $\Sigma_1$ [Fig. 5(b)], according to the experiments, the bond-bending branches are located in the 30 to 60 meV frequency region and the bond-stretching one lies between 60 and 75 meV. The structure factor analysis for $\boldsymbol{\tau} = (330)$ predicts the largest intensities for the Mn-O bond-bending mode going from 30 meV at $\Gamma$ to 50 meV at the zone boundary, while undergoing several branch crossings. It can be undoubtedly assigned to the measured data denoted by the filled symbols. The measured frequency at $\approx$59 meV at the zone boundary belongs to an additional branch (bond-bending mode character) that shows nonzero structure-factor intensities for $\xi \geqslant 0.3$. For the case $\boldsymbol{\tau} = (440)$ theory predicts a complex branch crossing scenario involving three different modes. At $\Gamma$, the main intensity is located at the lower branch at roughly 40 meV, which then halfway to M is transferred to the upper branch at about 60 meV. In this energy range, experimental spectra generally displayed a multipeak structure. However, if one follows the position of the main intensity peak as indicated by the dashed line in the right panel of Fig. 5(b), a similar $q$ dependence is found.[12] For the high-frequency bond-stretching branch (above 60 meV) theory predicts a downward dispersion in agreement with experiment for $\xi \leqslant 1/4$, but then shows a minimum followed by an upward bending. This seems to be in contrast to the measured plateau at around 60 meV for $0.3 \leqslant \xi \leqslant 0.4$. Unfortunately, near the zone boundary this frequency range (around 65–70 meV) was not entirely scanned

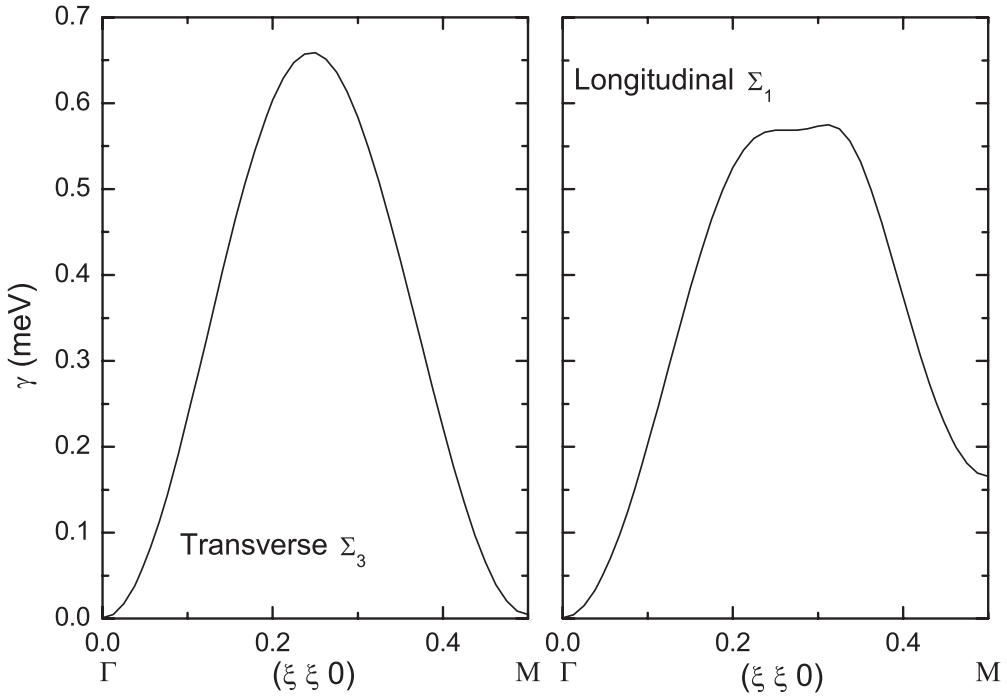


FIG. 6. Calculated e-ph induced linewidths $\gamma_{\mathbf{q}\lambda}$ (half-width at half-maximum) of the high-frequency Mn-O bond-stretching modes for both transverse $\Sigma_3$ and longitudinal $\Sigma_1$ polarizations in the FM phase.

in the experiment. In addition, calculated structure factors suggest that for both reciprocal lattice vectors considered in the measurements[12] the maximum scattering intensity at the zone boundary does not correspond to the bond-stretching branch. Regarding this and the rather poor energy and momentum resolution in these high-energy scattering experiments, it is possible that this branch is hidden by a more intense lower energy peak in the same **q** region. Currently we are establishing a set of wave vectors where theory predicts optimal conditions to resolve this issue, that is, determining the zone boundary frequencies of the $\Sigma_1$ and $\Sigma_3$ zone boundary phonons.

In this context it is interesting to note that the downward dispersion of the longitudinal bond-stretching branch could not be reproduced by the shell model,[12] which predicted an upward dispersion. Our NM calculations give a similar wrong upward dispersion, while the description of the downward dispersion is essentially recovered for the FM phase. This suggests that the shell model does not properly catch the effect of magnetism on the vibrational properties.

### D. Electron-phonon coupling

As discussed by Weber *et al.* (Ref. 12), e-ph coupling provides a link between phonon renormalization in the low-temperature metallic phase and the high-temperature polaronic insulating phase. We have calculated the e-ph induced phonon linewidth $\gamma_{\mathbf{q}\lambda}$ (half-width at half-maximum) in the FM phase for all modes with $q_z = 0$. We found that by far the largest $\gamma_{\mathbf{q}\lambda}$ are obtained for the high-frequency branches related to the Mn-O bond-stretching vibration. Exemplary, in Fig. 6 we present $\gamma_{\mathbf{q}\lambda}$ for these branches of transverse $\Sigma_3$ and longitudinal $\Sigma_1$ polarizations (similar results are obtained for the corresponding branches of $\Sigma_2$ and $\Sigma_4$ symmetry). They all exhibit a maximum between $\xi = 0.25$ and $\xi = 0.30$, which is the same region where the dip in the phonon dispersion occurs. This confirms that the dip structure is related to a renormalization via electron-phonon coupling. The same qualitative $q$ dependence for the linewidth of the bond-stretching mode was observed experimentally, albeit with larger values.[12] However, we found that the overall e-ph coupling is only moderate. The e-ph coupling parameter $\lambda$ averaged over all modes with $q_z = 0$ gives a value of 0.65, which implies medium coupling.

## IV. CONCLUSIONS

We have performed a first-principles linear-response study of the lattice dynamical properties for the tetragonal double-layer manganite system $La_{2-2x}Sr_{1+2x}Mn_2O_7$ ($x = 0.4$) for both the ferromagnetic (FM) and nonmagnetic (NM) phases in the $q_z = 0$ plane using the low-temperature experimental crystal structure. Comparison of the FM and NM phonon spectra reveals that the presence of magnetic order influences in particular the dispersion of high-frequency modes in the 60–75 meV range. The corresponding zone-boundary phonon modes involve predominantly bond-stretching type vibrations of oxygen atoms of the MnO octahedra. An analysis of real-space force constants reveals that not the nearest-neighbor Mn-O bonds, but longer Mn-Mn, O-O, and Mn-O bonds are modified in their dynamical couplings by the magnetic order. The changes can be linked to the type of Mn $d$ orbitals present at the Fermi level, which changes from $d(t_{2g})$ for the NM case to $d(e_g)$ for the FM phase. This strengthens the Mn-Mn bonds and weakens the others, provoking a strong nonmonotonous effect of magnetism on the high-frequency vibrational properties of this double-layer manganite. Structure factor analysis

of the [110] phonon dispersion for the FM phase showed good agreement with the findings of a previous inelastic neutron scattering experiment in the low-temperature FM phase, and allowed a clear assignment of measured branches to the Mn-O bond-bending and bond-stretching modes. Finally, the dip in the bond-stretching dispersion halfway between Γ and M is found to be connected with enhanced electron-phonon coupling, albeit the average coupling constant $\lambda = 0.65$ puts this double-layer manganite in the medium coupling regime.

## ACKNOWLEDGMENTS

This research was supported by the Karlsruher Institut für Technologie (KIT), Germany and by Bilateral Cooperation in Education and Research (MEX 09/008) of the International Bureau of the BMBF (German Federal Ministry of Education and Research). We thank F. Weber for useful discussions. One of the authors (O.D.-S.) gratefully acknowledges the Consejo Nacional de Ciencia y Tecnología (CONACYT, México) and the Deutscher Akademischer Austausch Dienst (DAAD).

[1] R. von Helmolt, J. Wecker, B. Holzapfel, L. Schultz, and K. Samwer, Phys. Rev. Lett. **71**, 2331 (1993).
[2] S. Jin, H. M. O'Bryan, T. H. Tiefel, M. McCormack, R. A. Fastnacht, R. Ramesh, and L. H. Chen, Science **264**, 413 (1994).
[3] M. B. Salamon and M. Jaime, Rev. Mod. Phys. **73**, 583 (2001).
[4] D. M. Edwards, Adv. Phys. **61**, 5 (2002).
[5] K. Momma and F. Izumi, J. Appl. Crystallogr. **41**, 653 (2008).
[6] R. Seshadri, A. Maigan, M. Hervieu, N. Nguyen, and B. Raveau, Solid State Commun. **101**, 453 (1997).
[7] M. Kubota, H. Fujioka, K. Ohoyama, Y. Moritomo, H. Yoshizawa, and Y. Endoh, J. Phys. Soc. Jpn. **69**, 1606 (2000).
[8] Y. Moritomo, A. Asamitsu, H. Kuwahara, and Y. Tokura, Nature (London) **380**, 141 (1996).
[9] J. F. Mitchell, D. N. Argyriou, A. Berger, K. E. Gray, R. Osborn, and U. Welp, J. Phys. Chem. B **105**, 10731 (2001).
[10] X. J. Chen, C. L. Zhang, C. C. Almasan, J. S. Gardner, and J. L. Sarrao, Phys. Rev. B **67**, 094426 (2003).
[11] Z. Sun, Y. D. Chuang, A. V. Fedorov, J. F. Douglas, D. Reznik, F. Weber, N. Aliouane, D. N. Argyriou, H. Zheng, J. F. Mitchell, T. Kimura, Y. Tokura, A. Revcolevschi, and D. S. Dessau, Phys. Rev. Lett. **97**, 056401 (2006).
[12] F. Weber, N. Aliouane, H. Zheng, J. F. Mitchell, D. N. Argyriou, and D. Reznik, Nat. Mater. **8**, 798 (2009).
[13] W. E. Pickett and D. J. Singh, Phys. Rev. B **53**, 1146 (1996).
[14] P. Ravindran, A. Kjekshus, H. Fjellvag, A. Delin, and O. Eriksson, Phys. Rev. B **65**, 064445 (2002).
[15] D. J. Singh and W. E. Pickett, Phys. Rev. B **57**, 88 (1998).
[16] P. K. de Boer and R. A. de Groot, Phys. Rev. B **60**, 10758 (1999).
[17] Z. Sun, J. F. Douglas, D. S. Dessau, Q. Wang, A. V. Fedorov, H. Lin, S. Sahrakorpi, B. Barbiellini, R. S. Markiewicz, A. Bansil, H. Zheng, and J. F. Mitchell, Phys. Rev. B **78**, 075101 (2008).
[18] R. Saniz, M. R. Norman, and A. J. Freeman, Phys. Rev. Lett. **101**, 236402 (2008).
[19] X. Y. Huang, O. N. Mryasov, D. L. Novikov, and A. J. Freeman, Phys. Rev. B **62**, 13318 (2000).
[20] P. E. Mijnarends, S. Kaprzyk, B. Barbiellini, Y. Li, J. F. Mitchell, P. A. Montano, and A. Bansil, Phys. Rev. B **75**, 014428 (2007).
[21] J. W. Kohn and L. J. Sham, Phys. Rev. **140**, A1133 (1965).
[22] B. Meyer, C. Elsässer, F. Lechermann, and M. Fähnle, FORTRAN90 Program for Mixed-Basis Pseudopotential Calculations for Crystals, Max-Planck-Institut für Metallforschung, Stuttgart (unpublished).
[23] O. De la Peña-Seaman, R. de Coss, R. Heid, and K. P. Bohnen, Phys. Rev. B **79**, 134523 (2009).
[24] S. G. Louie, K. M. Ho, and M. L. Cohen, Phys. Rev. B **19**, 1774 (1979).
[25] S. Baroni, P. Giannozzi, and A. Testa, Phys. Rev. Lett. **58**, 1861 (1987).
[26] P. Giannozzi, S. de Gironcoli, P. Pavone, and S. Baroni, Phys. Rev. B **43**, 7231 (1991).
[27] R. Heid and K. P. Bohnen, Phys. Rev. B **60**, R3709 (1999).
[28] R. Heid, K. P. Bohnen, and K. M. Ho, Phys. Rev. B **57**, 7407 (1998).
[29] D. Vanderbilt, Phys. Rev. B **32**, 8412 (1985).
[30] V. Ozolins and M. Korling, Phys. Rev. B **48**, 18304 (1993).
[31] J. P. Perdew, K. Burke, and M. Ernzerhof, Phys. Rev. Lett. **77**, 3865 (1996).
[32] K. Kokko and M. P. Das, J. Phys.: Condens. Matter **10**, 1285 (1998).
[33] C. Zenner, Phys. Rev. **81**, 440 (1951).
[34] C. Zenner, Phys. Rev. **82**, 403 (1951).
[35] A. J. Millis, P. B. Littlewood, and B. I. Shraiman, Phys. Rev. Lett. **74**, 5144 (1995).
[36] P. G. de Gennes, Phys. Rev. **118**, 141 (1960).